Bulletin of the Seismological Society of America, Vol. 92, No. 4, pp. 1318–1332, May 2002

Study of the 1999 *M* 7.1 Hector Mine, California, Earthquake Fault Plane by Trapped Waves

by Yong-Gang Li, John E. Vidale, Steven M. Day, David D. Oglesby, and the SCEC Field Working Team

Abstract We recorded fault-zone trapped waves from aftershocks on portable seismometers in a tight linear array across the Lavic Lake fault, which was one of several faults that ruptured in the *M* 7.1 Hector Mine, California, earthquake on 16 October 1999. Trapped waves with large amplitudes and long duration at 4 to 7 Hz produced by aftershocks occurring within the rupture zone were recorded at stations close to the fault trace. However, the *S* waves registered at stations farther from the rupture zone for the same events were much briefer. Trapped waves recorded at the Hector Mine rupture zone are similar to those observed in the Landers rupture zone [Li *et al.*, 1994a,b], but show higher frequencies. Simulations of these trapped waves indicate a 75 to 100-m-wide low-velocity and low-*Q* waveguide along the Hector Mine rupture zone in which the *S* velocity is reduced by about 40% to 50% from wall-rock velocities, and *Q* is 10 to 60 in the depth range from the surface to ~10 km.

We interpret this low-velocity waveguide as being a remnant of the process zone formed by inelastic deformation around the propagating crack tip during dynamic rupture in the 1999 Hector Mine earthquake. The reductions of velocities and *Q* within the Hector Mine rupture zone are similar to those within the Landers rupture zone, suggesting that the fault-zone rock was damaged to the same degree in the two earthquakes. The wave-guide width (75–100 m) on the Hector Mine rupture zone (~40 km in the total length) is half that (150–250 m) of the Landers rupture zone (~80 km in the total length), consistent with the scaling of process zone size to rupture length as predicted in some published dynamic rupture models. Locations of aftershocks for which we observed trapped waves show bifurcation of the northern Hector Mine rupture at depth, although only the west rupture branch broke to the surface.

Introduction

The major crustal faults that accommodate tectonic motion are complex sets of slip planes, which probably are influenced by the presence of fault gouge and fluid, and exhibit deformation that ranges from steady to stick slip (Scholz, 1990). Observations suggest that fault zone complexity may segment fault zones (Aki, 1984; Malin *et al.*, 1989; Beck and Christensen, 1991) or control the timing of moment release in earthquakes (Harris and Day, 1993; Wald and Heaton, 1994). Geometrical, structural, and rheological fault discontinuities caused by spatial and temporal variations in strength and stress will affect the earthquake rupture (e.g., Das and Aki, 1977; Rice, 1980; Ellsworth, 1990; Blanpied *et al.*, 1992; Vidale *et al.*, 1994). Rupture segments are often related to fault bends, stepovers, branches, and terminations that have been recognized by surface mapping (e.g., Sieh *et al.*, 1993; Johnson *et al.*, 1994), exhumation (e.g., Chester *et al.*, 1993) or by seismic profiling and tomography (e.g., Thurber *et al.*, 1997; Lees and Malin, 1990; Michelini and McEvilly, 1991; Michael and Eberhart-Phillips, 1991).

The fine structure of the San Andreas fault at Parkfield and the San Jacinto fault near Anza at seismogenic depths has been investigated through fault-zone trapped waves (e.g., Li *et al.*, 1990, 1997; Jongmans and Malin, 1995; Li and Vernon, 2001). Since the trapped waves arise from coherent multiple reflections at the boundaries between the low-velocity fault zone and the high-velocity surrounding rock, these waves are able to probe the internal structure of the fault zone with high resolution (Li and Leary, 1990; Leary *et al.*, 1991; Li and Vidale, 1996; Ben-Zion, 1998). Trapped waves have been used to resolve the fine structures and continuity of rupture zones in recent major earthquakes at Landers, California (Li *et al.*, 1994a,b, 1999, 2000; Hough

et al., 1994), and Kobe, Japan (Li *et al.*, 1998b). At Landers, trapped waves revealed an approximately 200-m-wide wave guide along surface breaks of the rupture zone. Within the wave guide, seismic velocities are reduced by 40%–50% with Q of 10–50 in the depth range between surface and 10 km. We interpreted this low-velocity wave guide as partly the transitory result of the dynamic rupture in the 1992 M 7.3 earthquake, although it probably also represents the accumulated wear from many previous earthquakes. We also found that the Landers rupture zone underwent healing, in that the shear velocity within the rupture zone increased by ~2% between 1994 and 1998 after the mainshock (Li *et al.*, 1998a; Li and Vidale, 2001), supporting the existence of a broken-then-healing cycle in the history of earthquakes on the active faults.

The Hector Mine earthquake on 16 October 1999, is the second M 7+ quake with surface exposure in southern California in the past decades. It provides an excellent site for a fault-zone trapped wave study. The capture of fault-zone guided waves would give us more information about the internal structure of the rupture zone, the physical nature of fault segmentation, and the relationship between the fault zone structure and dynamic rupture process, as well as the healing of the fault after a major earthquake. The M 7.1 Hector Mine earthquake occurred in the eastern California shear zone, only 25 km northeast of the epicenter of the 1992 M 7.3 Landers earthquake. It produced a 40-km-long surface rupture involving portions of multiple fault zones. The two main faults involved are the Lavic Lake fault (LLF) and the Bullion fault (BF) (Fig. 1). This pattern of rupture along more than one mapped fault is similar to that from the Landers earthquake. On the LLF in the Bullion Mountains, the faulting with the maximum right-lateral strike slip of 5 m is relatively simple, with most of the slip on a single trace or on closely spaced parallel traces. This pattern is in contrast to the complex faulting pattern with minor slips in the southern and northern portions of the rupture zone (Treiman *et al.*, 2002).

Coordinated by the U.S. Geological Survey and with an aid of military trucks, we carried out a pilot seismic experiment at the north LLF in the Bullion Mountains for recording fault-zone trapped waves generated by aftershocks. We

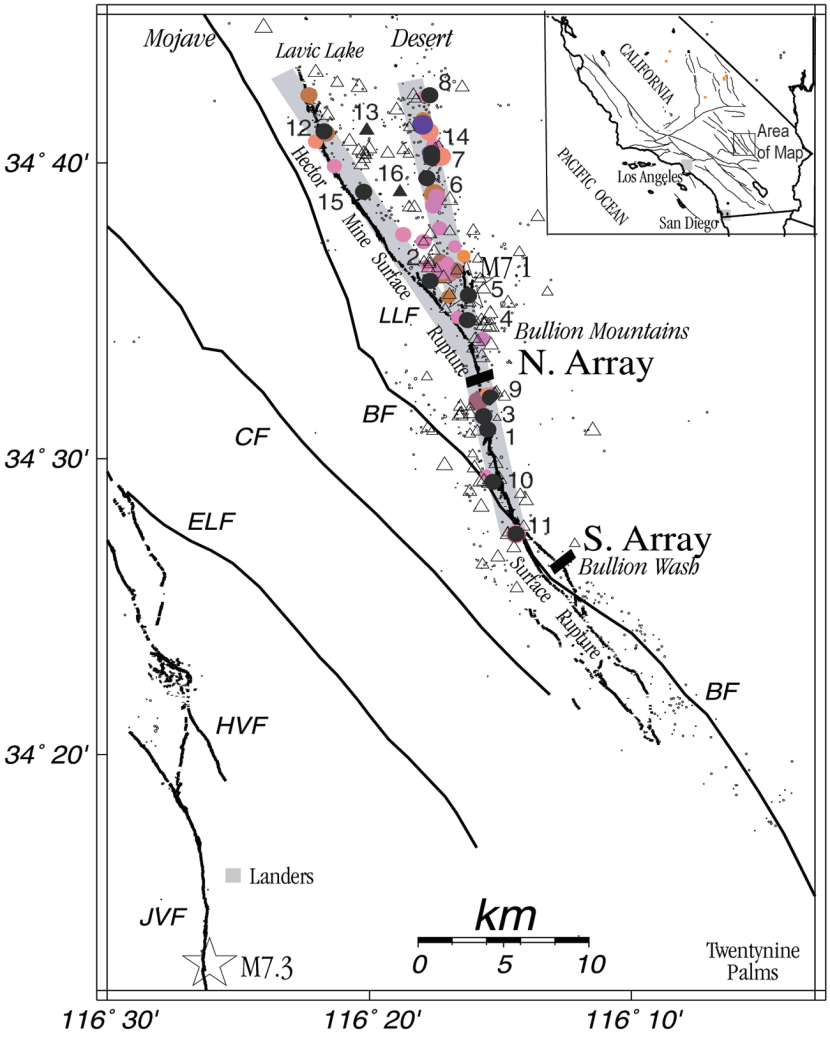

Figure 1. Map of the surveyed area showing locations of aftershocks and seismic arrays (solid lines) along the 1999 Hector Mine, California rupture zone. The inset shows the location of the area of map. Small dots: Hector Mine aftershocks that occurred in November of 1999. Circles and triangles: aftershocks showing and without prominent fault-zone trapped waves at the northern array. The size of symbols denotes the magnitude of events between M 1.5 and 3.0. Event depths, ranging from 2 to 12 km are coded by colors from red to blue. Black circles and triangles numbered 1 to 16: aftershocks whose waveforms are discussed in this article. BF, Bullion fault. CF, Calico Fault. ELF, Emerson Lake fault. HVF, Homestead Valley fault. JVF, Johnson Valley Fault. LLF, Lavic Lake fault. Shaded fault segments indicate the trapped-wave-inferred rupture zone of the 1999 Hector Mine earthquake. Surface ruptures along the LLF and southeast BF are also denoted in the map.

deployed a 60-channel Geometrics StrataView 24-bit exploration seismograph with 20 three-component sensors (Mark Products 2 Hz L22) provided by Program for Array Seismic Studies of the Continental Lithosphere (PASSCAL), on a 100-m-long line across the rupture zone 2 days after the mainshock (Li and Vidale, 2000). Outboard of the dense line, we placed two 6-channel Refraction Technology REFTEK recorders, each with two three-component sensors deployed at 75 m and 175 m away from the main fault trace on each side of the rupture zone. The recording site was located on volcanic rock above the region of greatest slip (4–5 m) in the mainshock, where the rupture zone is ~75 m wide, including one major and several parallel minor traces. We recorded 4- to 7-Hz fault-zone trapped waves with long-duration wave trains after *S* arrivals at stations located close to the main fault trace for aftershocks occurring within the rupture zone, but a much briefer *S* wave at a station 175 m away from the fault trace for the same events (Li, 2000). These trapped waves are similar to those observed at the Landers rupture zone in 1992 (Li *et al.*, 1994a,b).

To extend observations of fault-zone trapped waves in the Hector Mine rupture zone, the Southern California Earthquake Center (SCEC) organized an extensive deployment of 83 REFTEK seismometers belonging to PASSCAL and U.S. Geological Survey (USGS) at two sites on the north and south segments of the rupture zone in early November of 1999 (Fig. 1). The north seismic array was located at the same place in the Bullion Mountains where we obtained initial results from fault-zone trapped waves in our pilot experiment. The south array site was located in Bullion Wash, ~15 km south of the mainshock epicenter, where the rupture zone shows ~1-m right-lateral slip on the ground. At each site, we deployed a linear array across the fault trace. The southern array included a tight square-shape array of 20 stations on the east side of the fault trace for study of scattering of seismic waves from the fault zone. In approximately 3 weeks, hundreds of aftershocks with *P*-to-*S* time less than 3 sec were recorded at the two array sites.

In this article, we show fault-zone trapped waves recorded at the north seismic array deployed in November of 1999 and use trapped waves to delineate the northern portion of Hector Mine rupture zone at seismogenic depth. Locations of aftershocks for which we observed trapped waves show that the northern Hector Mine rupture zone bifurcated along two subparallel faults at depth in the Lavic Lake area, as opposed to the single slip plane on the middle rupture segment in the Bullion Mountains. The west rupture segment on the north LLF broke to the surface; the east rupture segment on a buried fault did not expose at the surface. This bifurcation of Hector Mine rupture zone suggested by fault-zone trapped waves is consistent with the seismicity pattern of aftershock locations (Hauksson *et al.*, 2002), and the rupture model of inversion of ground motion, telemetry, geodetic data, and surface breaks (Dreger and Kaverina, 2000; Ji *et al.*, 2002a,b; Simons *et al.*, 2000). We then used a 3D finite-difference code to synthesize trapped waves recorded at the northern seismic array in terms of a model with the realistic geometry of the fault zone and sources. The measured group velocities and *Q*-values of fault-zone trapped waves are used as constraints in the trapped wave modeling. Modeling of these trapped waves shows that shear velocities within the rupture zone are reduced by 40% to 50% from wall-rock velocities, similar to those within the Landers rupture zone. However, the width of the wave guide on the Hector Mine rupture zone is 70–100 m, about half that of the Landers rupture zone. The narrower wave guide on the Hector Mine rupture zone may correspond to the shorter rupture length of the Hector Mine earthquake, as predicted by rupture modeling (Cowie and Scholz, 1992).

Data Analysis

Figure 1 shows locations of the northern and southern seismic arrays deployed in the Bullion Mountains and Bullion Wash, respectively. The northern array included 20 stations along a 450-m-long line nearly perpendicular to the surface trace of the Lavic Lake fault (LLF) in the Bullion Mountains. The array site was near the 4-m right-lateral slip on the LLF. The station spacing of the array was not even (Fig. 2). Station ST0 at the center of the array was on the main fault trace. The southern seismic array was deployed at the rupture zone on the Bullion Fault in the Bullion Wash. The layout of the southern array was the same as the northern array, but combined with a tight square-shape array beside the fault trace. We used three-channel PASSCAL REFTEK

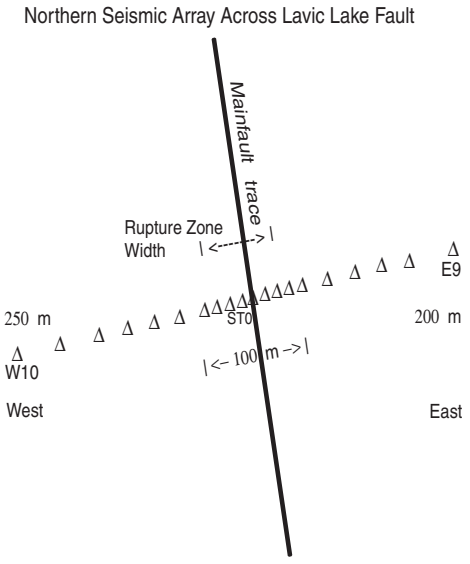

Figure 2. The layout of cross-fault seismic line at the northern array site in the Bullion Mountains. Station spacing is 12.5 m, for 9 stations in the middle part of the array, but 25 and 50 m for stations farther away from the main trace of the rupture zone. The rupture zone (marked by a dashed line) is ~75 m wide, including one major and several parallel minor traces, as well as many fissures on the ground surface.

recorders in the event-trigger mode. L22 sensors were buried with the three components aligned vertical, parallel, and perpendicular to the fault trace. The northern and southern seismic arrays crossed the fault trace at 34°32.37N, 116°15.79W, and 34°26.31N, 116°12.56W, respectively. In this article, we report the results from analysis of trapped waves recorded at the northern array in the Bullion Mountains. We plan to report the results from the data recorded at the southern array separately.

In November 1999, approximately 1000 aftershocks occurred in the Hector Mine epicentral region. Stations of the northern seismic array were well triggered by about 170 aftershocks with magnitudes *M* 1.6 to 3 and occurring at distances shorter than ~20 km from the array. We examined the data from these events for analysis of fault-zone trapped waves. We observed trapped waves from about 30 aftershocks among them. Locations of these events are shown in Figure 1. In this article, we present the waveform data from 16 aftershocks, for which locations and times are given in Table 1.

Figure 3 illustrates three-component seismograms at the northern array for 3 aftershocks (events 1, 2, and 3 in Fig. 1 and Table 1) that occurred with epicenters close to the rupture zone on the LLF. Events 1 and 3 were located 3 to 4 km south of the array at depths of 6.9 km and 10.3 km, event 2 was at the 6.2-km depth and ~6 km north of the array. Fault-zone trapped waves with relatively large amplitudes and long duration after *S* waves were recorded at stations close to the fault trace. In contrast, stations located farther away from the fault zone registered a much briefer *S* wave for the same events. The separation between the *S* waves and trapped waves for events 2 and 3 at the longer distance from the array was larger than for event 1, showing the existence of a low-velocity waveguide along the LLF.

Particle motions of three-component seismograms in a 2-sec time window after the *S* arrivals for these events (Fig. 4) show both Love-type and Rayleigh-type fault-zone trapped waves generated. We then calculated the amplitude spectra of trapped waves for a 2-sec time window starting from the *S* arrivals, using a Hanning window with a 60-msec taper. These spectra were normalized using coda waves to eliminate instrument, site, and source effects on the spectral amplitudes of trapped waves. The amplitude spectra of coda waves were calculated in a time window with the same length starting at 14 sec from the event origin time. Normalized trapped wave amplitude spectra showed a maximum peak at 4 to 5 Hz at stations located close to the mainshock fault trace for events 1 and 2 (Fig. 4). Trapped waves from the deeper event 3 showed peak amplitudes at 5–7.5 Hz, suggesting that the waveguide on the LLF is narrower at the deeper level. The maximum normalized spectral amplitudes of trapped waves from events 1, 2, and 3 are 100, 80, and 70, decreasing with the distance between the events and array along the Hector Mine rupture zone.

We observed fault-zone trapped waves at the northern seismic array for aftershocks occurring on the LLF that ruptured at the surface and also for aftershocks occurring along a line that directs more northerly from the mainshock epicenter. However, we did not observed trapped waves clearly at the same array for the aftershocks occurring between the LLF and this northerly directing line. For example, Figure 5 shows seismograms recorded for six aftershocks (events 6, and 12–16 in Fig. 1 and Table 1) occurring north of the mainshock epicenter at distances of 15 to 19 km from the array. Prominent trapped waves were recorded at stations close to the fault trace for events 12 and 15 occurring on the LLF and also for events 14 and 6 occurring along the northerly directing line. The event with the longer hypocentral

Table 1
Times and Locations of Hector Mine Aftershocks for Which Seismograms Are Shown in Figures

Event	Calendar Day	Date (mm/dd/yy)	Origin Time, UTC	Latitude, N	Longitude, W	Depth (km)	Magnitude	Range[a] (km)	Frequency[b] (Hz)
1	330	11/26/99	08:06:34.52	34°31.00′	116°15.48′	6.9	2.5	8	5
2	330	11/26/99	10:35:16.15	34°35.53′	116°16.21′	6.2	1.8	10	5
3	313	11/09/99	14:20:59.69	34°31.45′	116°15.63′	10.3	1.8	11	7
4	327	11/23/99	21:56:44.60	34°34.69′	116°16.25′	7.9	1.7	9	7
5	313	11/09/99	07:09:59.94	34°36.24′	116°16.92′	6.5	1.9	10	5
6	324	11/20/99	12:01:38.33	34°39.49′	116°17.79′	7.6	2.3	15	6
7	313	11/09/99	13:26:49.62	34°40.17′	116°17.62′	2.5	2.0	16	4
8	327	11/23/99	00:37:28.96	34°42.28′	116°17.68′	5.5	2.3	19	5
9	327	11/23/99	21:54:36.69	34°32.27′	116°15.28′	5.4	1.6	7	5
10	327	11/23/99	07:21:28.49	34°29.23′	116°15.49′	4.4	2.1	9	4
11	329	11/25/99	04:22:17.13	34°27.47′	116°14.60′	3.5	2.8	11	4
12	324	11/20/99	23:47:59.03	34°41.07′	116°21.84′	5.8	2.2	18	5
13	313	11/09/99	18:23:12.83	34°41.09′	116°20.09′	8.9	2.3	19	
14	313	11/09/99	12:15:19.42	34°40.34′	116°17.12′	4.0	2.2	17	6
15	315	11/11/99	23:49:29.76	34°39.03′	116°20.20′	7.7	2.3	15	6
16	316	11/12/99	11:02:04.56	34°39.02′	116°18.82′	11.9	1.5	16	

[a]The distance between the seismic array and the aftershock.
[b]The dominant frequency of trapped waves.

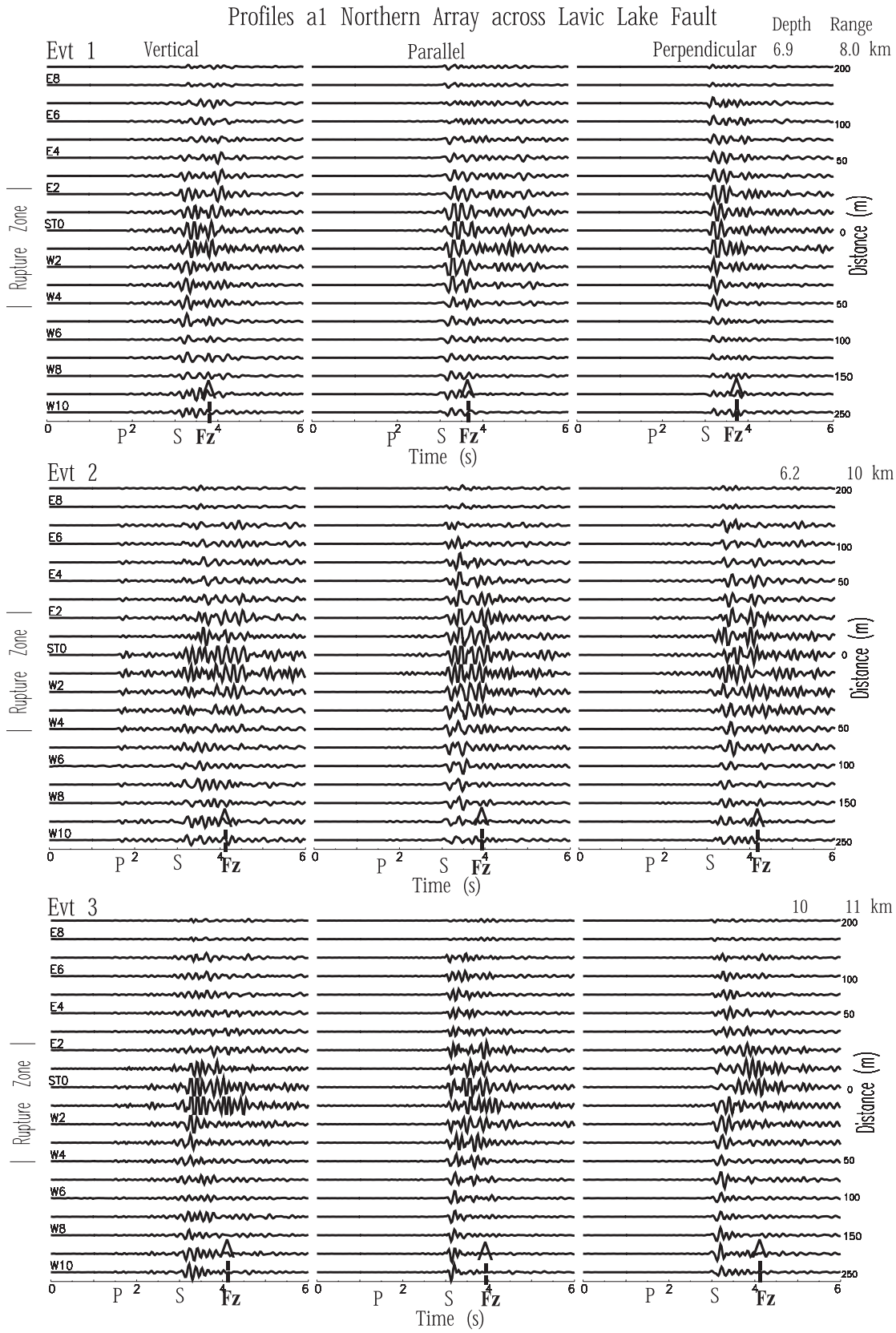

Figure 3. Vertical, fault-parallel, and fault-perpendicular seismograms recorded at the northern seismic array for three Hector Mine aftershocks (events 1, 2, and 3) occurring within the rupture zone. The focal depth and hypocentral distance (range) between the event and array are shown at upper right of the plot for each event. Station names beginning in E or W were located at the east or west side of the fault trace, respectively. Station ST0 was on the main fault trace. Station distance from the main fault trace is plotted at right of seismograms. Two solid bars mark the distance range in which fault-zone trapped waves are prominent. The recordings have been deconvolved by the sensor and instrument response. Seismograms are low-pass (<7 Hz) filtered and plotted using a fixed amplitude scale for all traces in each panel. P- and S-wave arrivals are denoted; *S* arrivals are aligned at 3 sec. Arrows denote the arrival of prominent fault-zone (Fz) trapped waves.

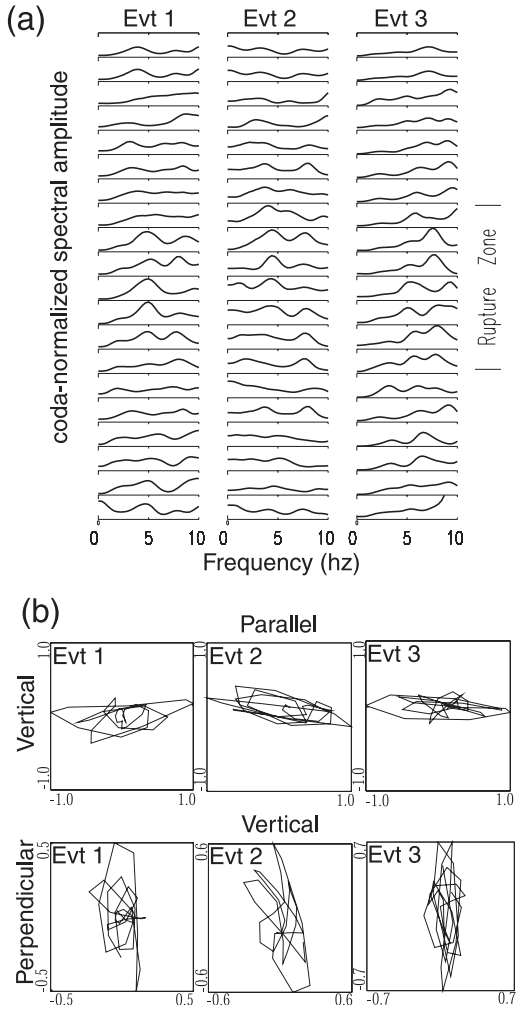

Figure 4. (a) Coda-normalized amplitude spectra of fault-parallel component trapped waves are plotted using a fixed amplitude scale of 100, 80, and 70 for events 1, 2, and 3. The peak amplitudes at 4–5 Hz appear at stations located within the rupture zone for events 1 and 2, but at 5–7.5 Hz for the deep event 3. (b) *Top*: Particle motion diagrams for vertical and fault-parallel component seismograms at station ST0 in a 2-s time window starting from *S* arrivals for events 1, 2, and 3. The *x* and *y*-axis scales are normalized to ± 1. *Bottom*: Particle motion diagrams for vertical and fault-perpendicular component seismograms. The *x*- and *y*-axis scales are normalized with respect to the scale for particle motion diagram in the top panel.

distance showed the greater time delay of trapped waves after *S* waves. However, no clear trapped waves were registered at the array for events 13 and 16, which occurred between the LLF and the northerly directing line. These observations show again the existence of a low-velocity wave guide on the LLF and also indicate the existence of another low-velocity wave guide on a buried fault directing northerly from the mainshock epicenter, which probably ruptured in the Hector Mine earthquake but did not break to the surface.

Figure 6 shows fault-parallel component trapped waves for 10 aftershocks occurring on the LLF and the buried fault at hypocentral distances of 7 to 19 km from the array. The duration of trapped wave trains after *S* waves increases roughly with hypocentral distances of these events, as expected for trapped waves traveling along the continuous slower fault zone. These observations confirm the existence of low-velocity wave guides on the LLF and also on the buried fault; both of them extend at least 15 km north of the mainshock epicenter (Fig. 1). We interpret the low-velocity wave guides on the LLF and the buried fault being associated with the rupture on them in the 1999 Hector Mine earthquake, although only the rupture on the LLF exposed at the surface. The seismicity pattern of Hector Mine aftershocks also indicate the bifurcation of northern rupture zone (Hauksson *et al.*, 2002). Fault-zone trapped waves generated by aftershocks occurring on the buried fault are roughly similar to those generated by aftershocks on the north LLF, from which we infer that the low-velocity wave guides on these two faults are similar at seismogenic depth. Joint inversion of strong-motion records, teleseismic body waves, Global Positioning System (GPS) displacement vectors, and geological surface breaks show the similar seismic moment releases on the two rupture segments along the north LLF and the buried fault (Ji *et al.*, 2002a,b).

The low-velocity wave guides on the north LLF and the buried fault connect in the Bullion Mountains and extend southward. Figure 6 also shows fault-zone trapped waves recorded at the northern array for three aftershocks (events 3, 10, and 11 in Fig. 1 and Table 1) occurring south of the array. Events 10 and 11 occurred at shallow depths of 4.4 and 3.5 km with epicenters at 7 and 10 km south of the array. Event 3 occurred at a depth of 10.3 km and 2 km south of the array. Prominent trapped waves were recorded at stations close to the fault trace for these aftershocks, showing that the low-velocity wave guide extends southward at least 15 km along the rupture on the LLF from the mainshock epicenter. However, we note that the deep event 3 shows a shorter duration of trapped wave trains after *S* waves than do shallow events 10 and 11, although the hypocentral distance between event 1 and the array is longer, indicating the depth-dependent velocity structure within the rupture zone.

To evaluate *Q*-values of the fault rock in the rupture zone, we plotted coda-normalized spectral amplitudes of trapped waves versus hypocentral distances for the 12 aftershocks in Figure 7. Normalized spectral amplitudes of trapped waves decrease with the hypocentral distance of events along the rupture zone. Spectral amplitudes for these events are taken from the computations of coda-normalized amplitude spectra of fault-parallel component seismograms (examples shown in Fig. 8). Each point in Figure 7 denotes the mean of spectral amplitude peaks between 4 and 7 Hz measured at 5 stations of the array located within the rupture zone. Error bars at denote the standard deviation of measurements. The large standard deviation may be due to the contamination of other phases, such as direct *S* waves in

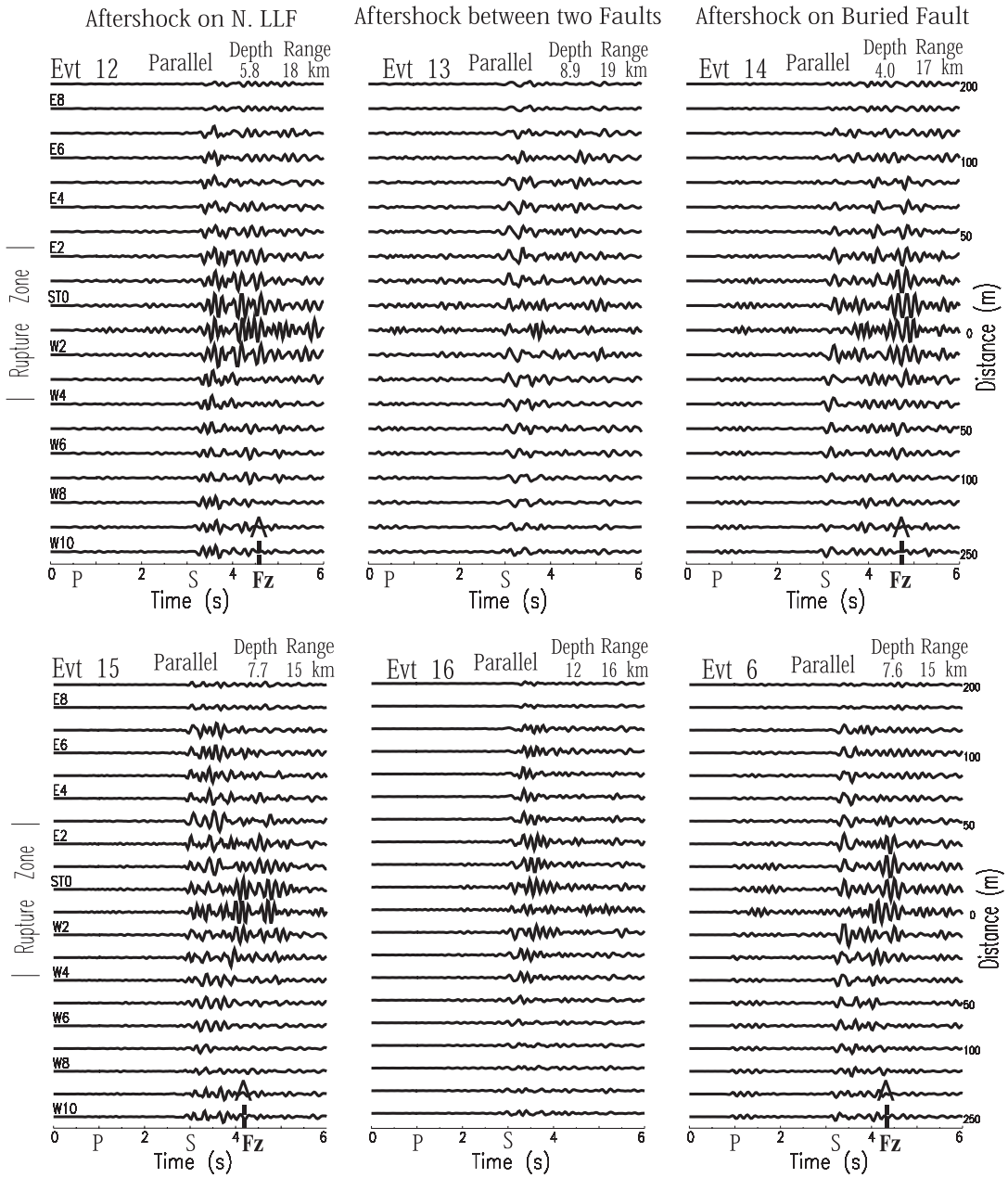

Figure 5. Fault-parallel component seismograms recorded at the northern array for 6 Hector Mine aftershocks (events 6 and 12–16). Events 12 and 15 occurred on the north Lavic Lake fault (LLF); events 6 and 14 occurred on the buried fault north of the mainshock epicenter; events 13 and 16 occurred between the LLF and buried faults. The depth and hypocentral distance of the event are plotted at upper right of each panel. Seismograms have been low-pass (<7 Hz) filtered and are plotted using a fixed amplitude scale for all traces in each panel. Prominent fault-zone trapped waves appeared at stations close to the fault trace for events occurring on the LLF and the buried fault, but not for the events occurring between the two faults. Other notations are as in Fig. 3.

seismograms, and the heterogeneity of the fault zone. We divided the data into two groups, the first group consisting of events 9, 10, 11, 7, and 14 occurring at depths shallower than 5.5 km and the second group consisting of events 1, 2, 3, 6, 15, 12, and 8 occurring at depths deeper than 5.5 km. We fit the data using the formula $\ln(A_1/A_i) = \pi f(r_i - r_1)/QV_s$, where A_i is the normalized spectral amplitude for the event located at distance r_i to the array and $i = 1, \ldots, 12$ for 12 events used in Figure 7. The amplitude A_i has been multiplied by a factor $1/\sqrt{r_i}$ to correct for geometrical spreading for trapped waves. For shallow events, shear velocity V_s is assumed to be 2.2 km/sec and frequency f is 4.5 Hz. For deep events, V_s is assumed to be 2.4 km/sec and f is 5.5 Hz. We obtained the best fit to the data using a Q of 30 for

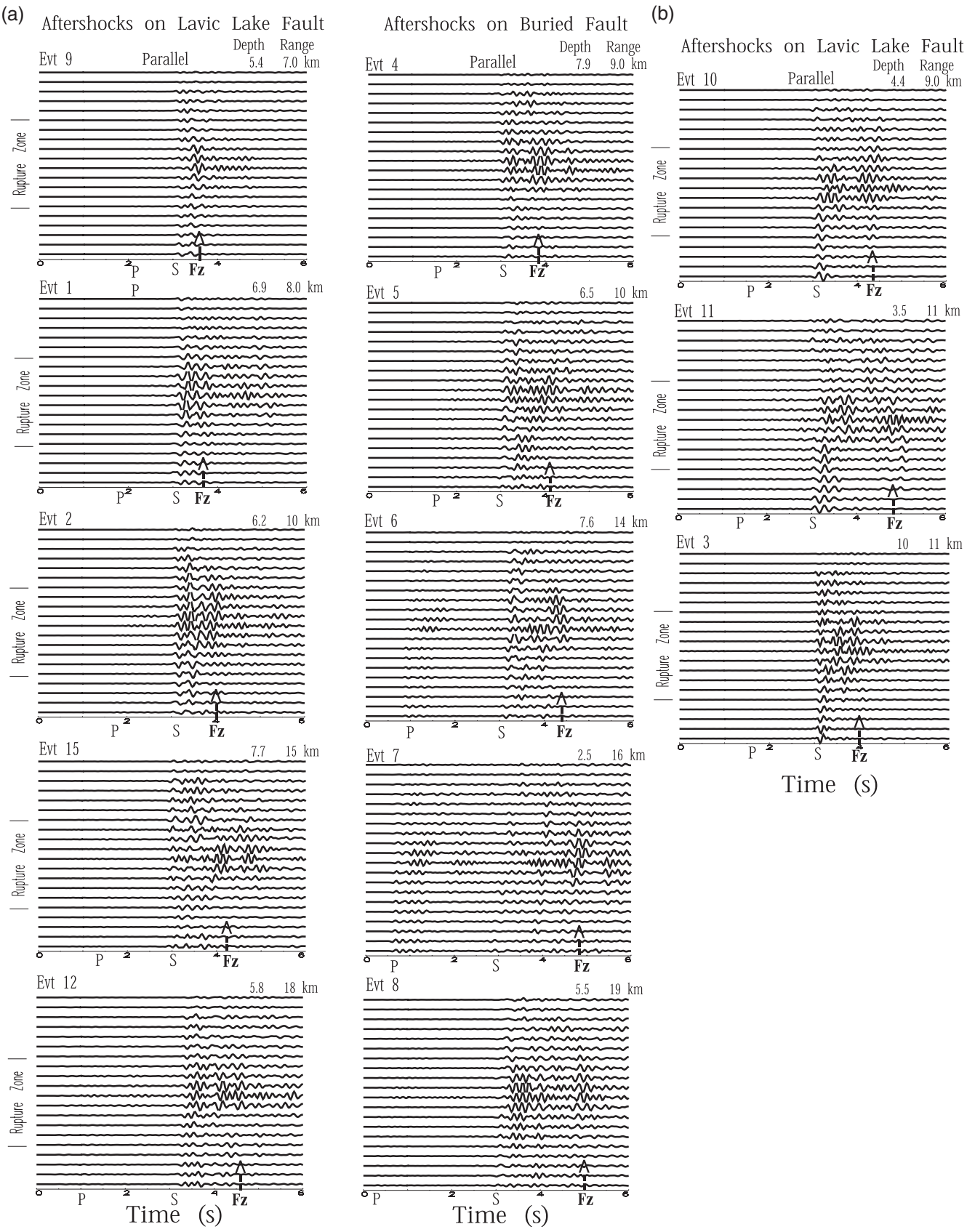

Figure 6. Fault-parallel component seismograms recorded at the northern array for 13 Hector Mine aftershocks occurring on the LLF and buried fault at hypocentral distances of 7 to 19 km from the array. Events 10, 11, and 3 occurred south of the array. Seismograms have been low-pass (<7 Hz) filtered and are plotted with *S*-wave arrivals aligned at 3 sec. Prominent fault-zone trapped waves (denoted by arrows) appear at stations within the rupture zone. Other notations are as in Fig. 3.

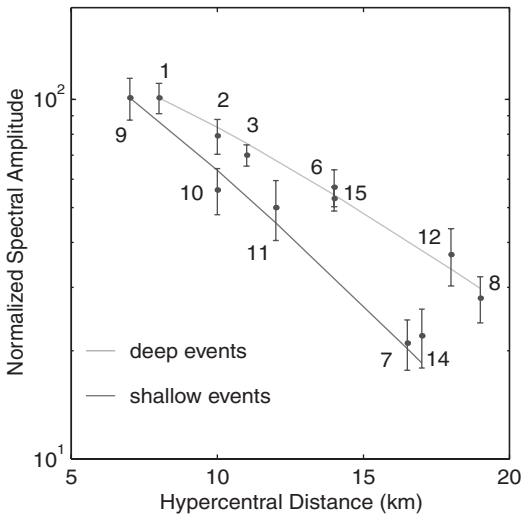

Figure 7. Normalized spectral amplitudes of trapped waves versus hypocentral distances for 12 Hector Mine aftershocks. Events are numbered. Each point denotes the mean of coda-normalized spectral amplitude peaks at 4–7 Hz at five stations within the rupture zone. Examples of coda-normalized spectra are shown in Figs. 4 and 8. We fit the data using the formula $\ln(A_1/A_i) = \pi f(r_i - r_1)/QV_s$. Spectral amplitudes of trapped waves are multiplied by a factor of $(r_i/r_1)^{1/2}$, $i = 1, \ldots, 12$, to correct for geometrical spreading. The solid line fits the data for shallow events 9, 10, 11, 7, and 14 using Q of 30; the light line fits the data for deep events 1, 2, 3, 6, 15, 12, and 8 using Q of 50.

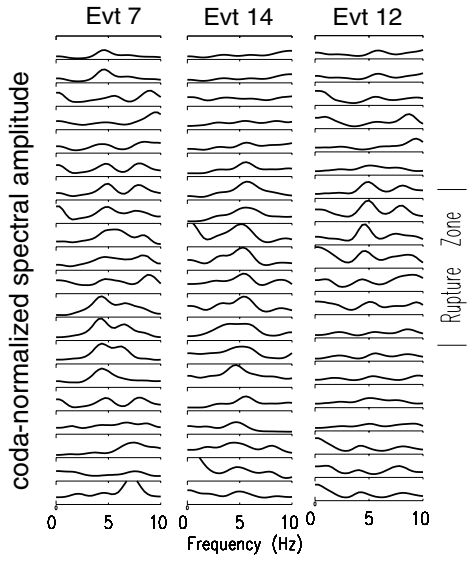

Figure 8. Coda-normalized amplitude spectra of trapped waves from events 7, 14, and 12 occurring within the Hector Mine rupture zone at hypocentral distances of 16, 17, and 18 km from the northern array. Data are plotted using a fixed amplitude scale of 20 for events 7 and 14 and a scale of 35 for event 12. The peak amplitudes at ~5 Hz appear at stations located within the rupture zone.

shallow events and a Q of 50 for deep events, showing that fault zone Q increases with depth. These Q-values are similar to those estimated for the Landers rupture zone (Li *et al.*, 2000).

To study the dispersion of trapped waves, we filtered seismograms using a four-pole butterworth filter with 0.5-Hz frequency band, where the center ranged from 1.75 to 5.75 Hz with a step of 0.5 Hz. For example, Figure 9 shows band pass-filtered seismograms recorded at station ST0 of the northern array for five aftershocks (events 1, 3, 5, 10, and 11) occurring within the rupture zone and at different depths and hypocentral distances. We also calculated the envelope of band pass-filtered seismograms using the Hilbert transform. The peak in envelope indicates the arrival time of the most energy in the specific frequency band. Multiple bandpass-filtered seismograms show the dispersion of trapped waves. Trapped waves at higher frequencies traveled more slowly than those at lower frequencies. We note that trapped waves from shallow event 11 occurring at a depth of 3.5 km show a greater time delay after S arrivals than those from deep event 3 occurring at a depth of 10.3 km, although the two events had the similar hypocentral distance to the array. We derived group velocities of trapped waves from multiple band-pass filtered seismograms for these aftershocks. Group velocities range from 2.0 km/sec at 5–6 Hz to 2.6 km/sec at 2 Hz for shallow events and from 2.4 km/sec at 5–6 Hz to 3.0 km/sec at 2 Hz for deep events, showing an increase in fault zone velocity with depth. These group velocities are used as velocity constraints in trapped wave modeling.

Simulations of Trapped Waves

We synthesized fault-zone trapped waves using a 3D finite difference code (Graves, 1996) that we have used for simulation of fault-zone trapped waves observed at the Landers rupture zone (Li *et al.*, 2000). First, we constructed a 3D model with the depth-variable structure for the Hector Mine rupture zone constrained by the regional velocity model, and group velocities and apparent Q-values from trapped waves. This model is similar to the velocity model of the Landers rupture zone. We then refined model parameters in a trial-and-error modeling procedure to best fit seismograms from 16 Hector Mine aftershocks occurring within the rupture zone at different depths and distances from the northern seismic array.

A depth-dependent fault zone structure is expected because the increasing pressure with increasing depth will strongly affect the crack density, fluid pressure, and amount of fluids, as well as the rate of healing of damage caused by earthquakes (Sibson, 1977, 1983; Byerlee, 1990; Rice, 1992). It may also influence the development of fault gouge (Scholz, 1990; Marone, 1998a, b). For all these reasons, a realistic fault zone is probably not uniform with depth.

The 3D finite-difference computer code is second order in time and fourth order in space. It propagates the complete

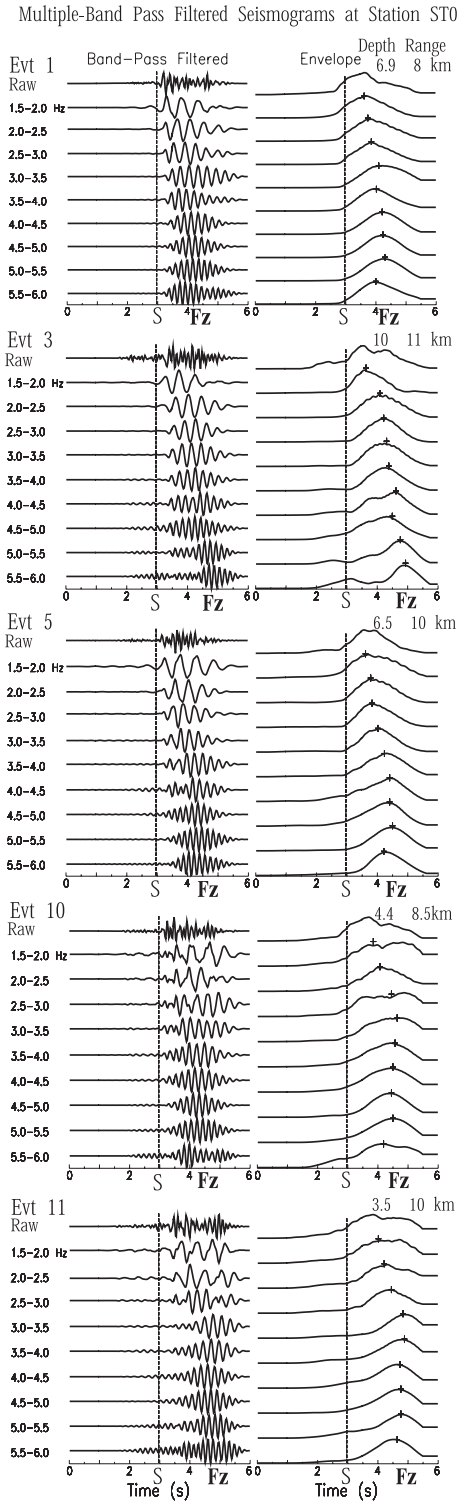

Figure 9. left: Multiple band-pass filtered fault-parallel seismograms at station ST0 of the northern array for events 1, 3, 5, 10, and 11. Depths and hypocentral depths of these events are plotted at upper right of each panel. Seismograms are filtered in 9 frequency bands between 1.5 and 6.0 Hz and plotted in trace-normalized. *S* arrivals for the events are aligned at 3 sec. Multiple band-pass filtered seismograms show the dispersion of trapped waves. right: Computed envelopes of band-pass filtered seismograms using a Hilbert transformation. The peak of envelope with a cross indicates the arrival of energy at the specified frequency band.

wave field through elastic media with a free-surface boundary and spatially variable anelastic damping (an approximate *Q*). The calculation used a 100-by-800-by-800 element grid in *x*–*y*–*z* coordinates with the grid spacing of 12.5 m to simulate a volume of 1.25 km in width, 10 km in length, and 10 km in depth. For the events with larger distance from the array, we need to increase the grid volume. The fault-zone wave guide is sandwiched between two quarter-spaces, and placed down the middle of the grid. The double-couple sources were used.

To find model parameters that best fit observed trapped waves, we tested various values for the fault zone width, velocity, and *Q*; the wall-rock velocity and *Q*; the layer depths; and the source location. These parameters trade off each other in modeling, so they are not uniquely determined. This problem has been discussed in previous studies for a delineation of fault zone structure using trapped waves (e.g., Li and Leary, 1990; Leary *et al.*, 1991b; Li and Vidale, 1996; Ben-Zion, 1998). However, the trade-offs among the parameters can be reduced when we have independent estimates of some parameters to use as constraints in modeling, such as group velocities and *Q*-values estimated from the dispersion and attenuation of trapped waves. We also used the velocity model of the Landers rupture zone as a starting model because the Hector Mine rupture zone is only ~25 km away from the Landers rupture zone in the Eastern California Shear Zone. In previous articles on modeling of trapped waves observed at the Landers rupture zone [Li *et al.*, 1999, 2000], we have given examples to show the sensitivity of these model parameters to synthetic trapped waveforms. A wider fault zone produces trapped waves with lower frequencies, and a slower fault zone produces longer dispersive wave trains of trapped waves. A lower-*Q* fault zone produces trapped waves with smaller amplitudes and shorter wave trains at lower frequencies. The variation of wall-rock velocities and layer depths affects the arrival times of *P* and *S* waves, but variation of wall-rock *Q* produces minimal variation in modeling results.

Figure 10 shows the depth section of the structure model across the Hector Mine rupture zone on the Lavic Lake fault in Bullion Mountains. The fault-zone wave guide is 100 m wide at surface and tapers to 75 m at the depth of 10 km. The shear velocities within the fault zone are reduced by 40%–50% from wall rock velocities and *Q* is 10–60. Table 2 gives the model parameters that we used to generate synthetic fault-zone trapped waves best fit to the data.

For example, Figure 11 shows 3-D finite-difference synthetic three-component seismograms at the northern array across the Hector Mine rupture zone for two aftershocks (events 1 and 2) occurring at depths of 6 to 7 km within the rupture zone, 3 km south, and 7.5 km north of the northern seismic array, respectively. Event 2 was located near the mainshock epicenter. The model parameters are given in Figure 10 and Table 2. Fault-zone trapped waves that have long wave trains with dispersion following *S* waves are concentrated within the fault zone. The trapped waves from

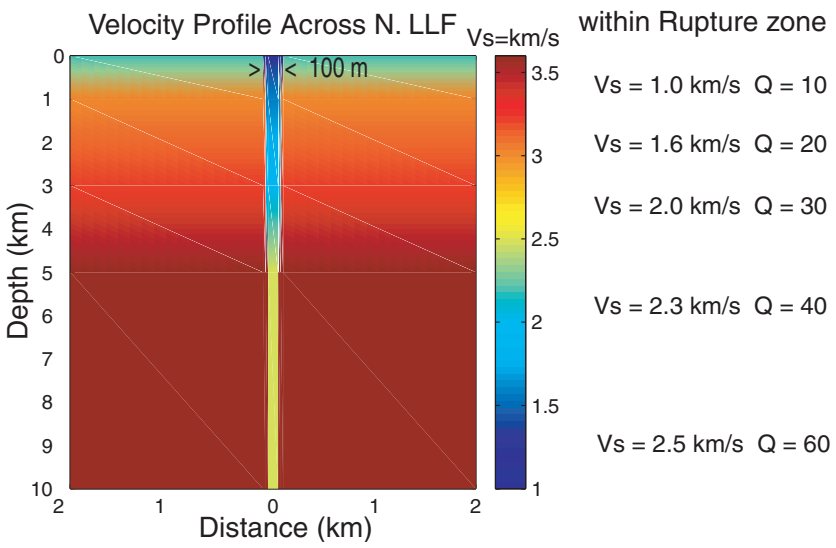

Figure 10. The depth section of structure model across the Hector Mine rupture zone in the Bullion Mountains. The rupture zone is 100 m wide at the surface and tapered to 75 m at the depth of 10 km. Depth-dependent velocities and *Q*-values within the waveguide are shown in the figure, which are used for the best fit to the data. Shear velocities within the rupture zone are reduced by 50% to 40% from wall-rock velocities between the surface and 10 km depth.

Table 2
Model Parameters for the Hector Mine Rupture Zone

	Best Fit				
Model parameters	Layer 1	Layer 2	Layer 3	Layer 4	Layer 5
Depth of the layer bottom, km	1.0	3.0	5.0	8.0	10.0
Waveguide width, m	100	100	75	75	75
Waveguide *S* velocity, km/s	1.0	1.6	2.0	2.3	2.5
Waveguide *Q*-value	10	20	30	40	60
Wall-rock velocity, km/sec	2.0	3.0	3.3	3.5	3.7
Wall-rock *Q*-value	20	40	60	100	120

event 2 show longer duration of wave trains than those from event 1 because of the greater distance between event 2 and the array. Synthetic seismograms are comparable with observations. We notice that the goodness of fit to three-component seismograms is not the same, probably because of anisotropy of fault-zone rocks, which is not included in the model.

Figure 12a shows fault-parallel component synthetic and observed seismograms at the northern seismic array for three aftershocks, event 15 occurring within the west rupture segment on the north LLF, event 6 occurring within the east rupture segment on the buried fault, and event 16 occurring between the two rupture segments at distances of 15 to 16 km north of the array. We used the same model parameters for the waveguides on the LLF and the buried fault. The double-couple source is located within the low-velocity wave guide for events 15 and 6, but 1.5 km away from the wave guide for event 16. Prominent fault-zone trapped waves with large amplitudes and long duration wave trains are generated by events 15 and 6, but not by event 16. The simulations of trapped waves for these three events are consistent with observations, showing the bifurcation of the northern Hector Mine rupture zone on the LLF and the buried fault north of the mainshock epicenter.

In Figure 12b, we illustrate examples of 3D finite-difference synthetic seismograms for three aftershocks occurring within the rupture zone on the LLF south of the northern seismic array at hypocentral distances of 9–11 km from the array. We note that trapped waves from shallow events 10 and 11 show a longer duration after *S* waves than those from deep event 3, because of the depth-dependent velocity structure within the rupture zone. We obtain a good agreement between synthetics and observations, showing that the model in Figure 10 and Table 2 can explain the structure of the Hector Mine rupture zone.

We generate synthesized seismograms for all events in Table 1 using model parameters shown in Table 2. To obtain the best fit to observations in modeling, we change hypocentral distance of events up to 0.5 km from the value given by catalogs, allowing for location error and also the lateral heterogeneity along the fault zone. The model parameters given in Table 2 are not uniquely constrained by this forward modeling because there are trade-offs among them.

Discussions and Conclusions

The 1999 *M* 7.1 Hector Mine earthquake and the 1992 *M* 7.3 Landers earthquake in southern California provide excellent sites for recording fault-zone trapped waves. The two earthquakes occurred only ~25 km apart in the Eastern California Shear Zone and showed right-lateral strike-slip faulting and high stress drops (Wald and Heaton, 1994; Scientists of the USGS *et al.*, 2000). The Landers event produced surface breaks of total 80 km in the length with maximum slip of 7 m. The Hector Mine event produced 40-km-long surface breaks with maximum slip of 5 m.

Observations and models of fault-zone trapped waves from aftershocks allowed us to characterize the internal structure of rupture zones and the physical nature of fault segmentation with high resolution at the seismogenic depth. Trapped waves reveal a low-velocity zone (waveguide) to a

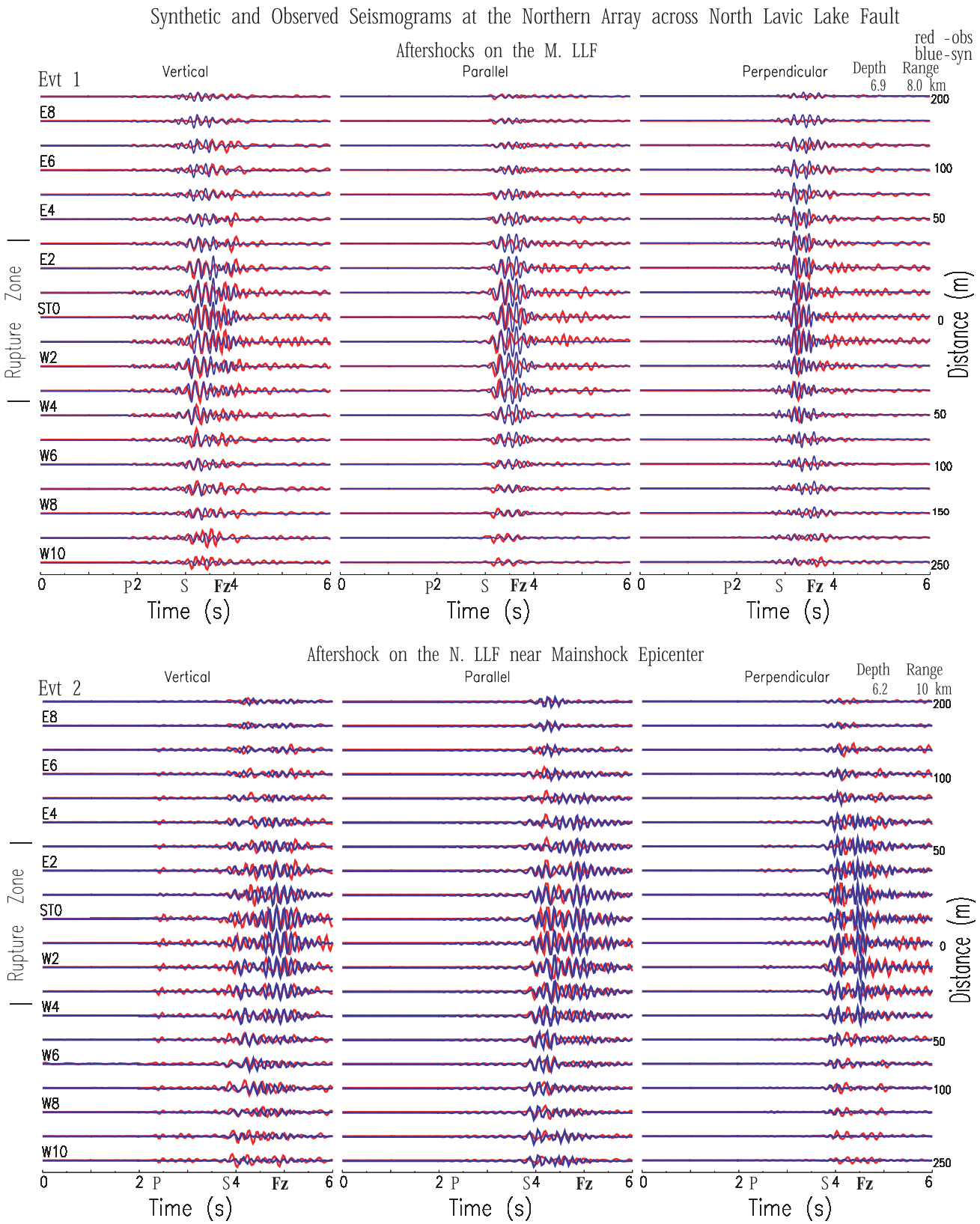

Figure 11. Three components of 3-D finite difference synthetic (blue lines) and observed (red lines) seismograms in cross-fault profiles at the northern array for two aftershocks (event 1 and event 2), using model parameters for the best fit given in Fig. 10 and Table 2. Trace spacings are the same as station spacings of the seismic array. A double-couple source is located within the low-velocity waveguide at the depth of 6.9 km and 3 km south of the profile for event 1, and at the depth of 6.2 km and 8 km north of the profile for event 5. The strike and rake angles are 0°, and dip angle is 90°. Synthetic and seismograms have been low-pass (<7 Hz) filtered and are plotted using a fixed amplitude scale in each plot. Trapped waves with relatively large amplitudes and long duration waveforms appear at stations within the fault zone. Other notations are as in Fig. 3.

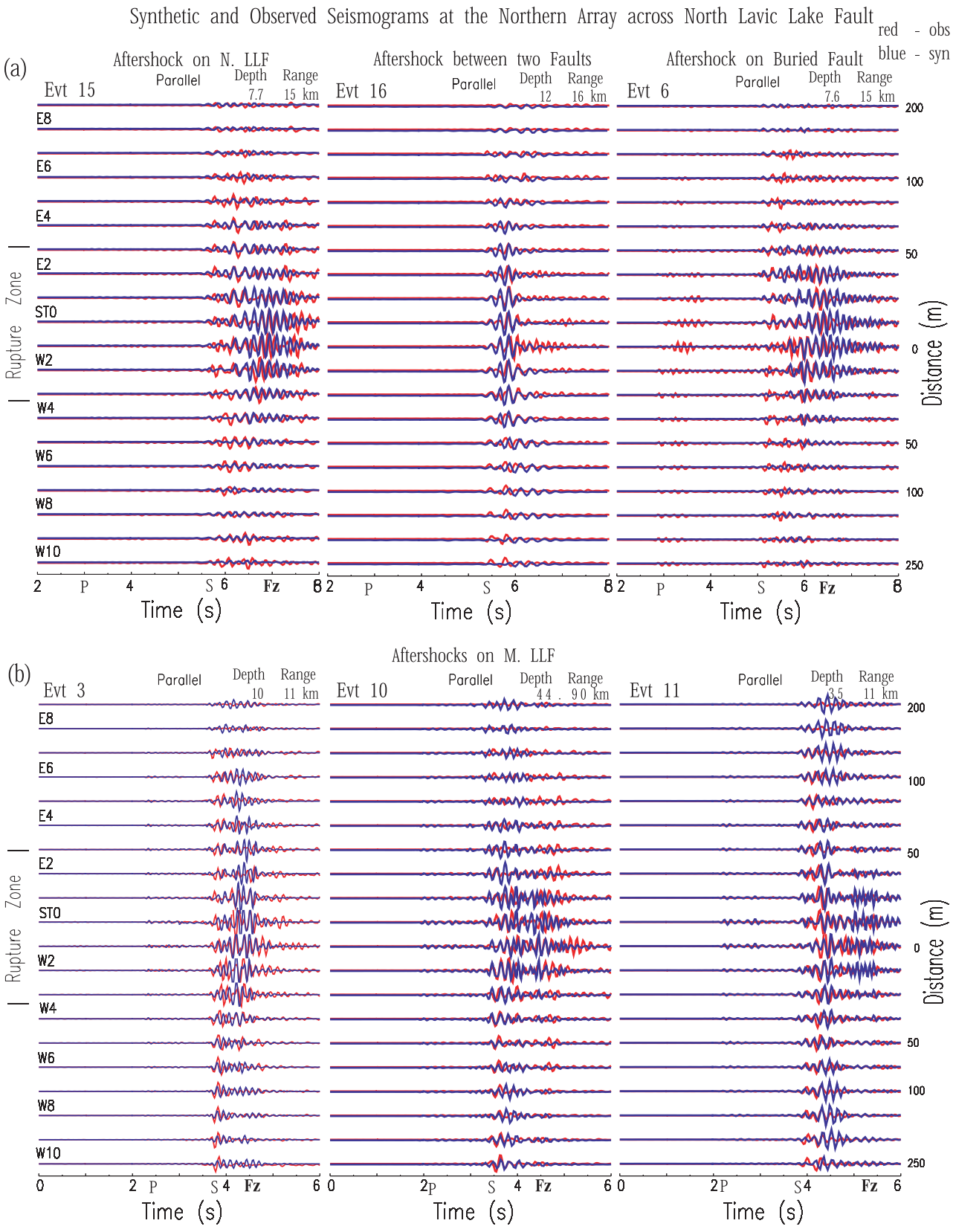

Figure 12. Fault-parallel component of 3-D finite-difference synthetic (blue lines) and observed (red lines) seismograms at northern array for three aftershocks (events 15, 16, and 6) occurring on the north Lavic Lake fault (LLF), the buried fault, and between them, respectively. Model parameters in Fig. 10 and Table 2 are used for simulations. A double-couple source is located within the waveguide for events 15 and 6, but 1.5 km away from the waveguide. Both synthetic and recorded seismograms have been low-pass ($<$7 Hz) filtered and normalized in each plot. Trace spacings of synthetics are the same as field station spacings. Fault-zone trapped waves are prominent at stations within the rupture zone for events 15 and 6, but not for event 16. (b) Fault-parallel component of 3-D finite-difference synthetic (blue lines) and observed (red lines) seismograms at the northern array for three aftershocks (events 3, 10, and 11) occurring within the rupture zone on the middle LLF. Other notations are as in Fig. 3.

depth of ~10 km along surface ruptures of the Hector Mine and Landers earthquakes, respectively. Within the waveguides, shear velocities are reduced by 40%–50% from wall-rock velocities and Q is 20–50, indicating that the damage degree of fault-zone rocks in the two earthquakes was similar. However, the waveguide width on the Hector Mine rupture zone is 75 to 100 m, only half the width (~200 m) on the Landers rupture zone (Li *et al.*, 1999, 2000).

From the point of view of fracture mechanics, the distinct low-velocity waveguides on the Hector Mine and Landers rupture zones may represent a remnant of the process zone, which is inelastic deformation around the propagating crack tip, as expected from theoretical work on existing fault-zone rupture models (e.g., Ida, 1973; Rice, 1980; Papageorgiou and Aki, 1983). It is reasonable that the wave guide could be softened by the dynamic rupture in the most recent major earthquake, although it more likely represents a wear zone that has accumulated over geological time. Repeated surveys using explosions at the Landers rupture zone have showed that the fault is healing (strengthening) after the 1992 M 7.3 earthquake (Li *et al.*, 1998a). The fault zone trapped waves recorded at the San Jacinto fault zone near Anza, California, showed the existence of a soft wave guide on the fault strand ruptured in the 1918 M 6.9 earthquake but the lack of a clear wave guide on the strands that did not break in the recent prehistoric times (Li *et al.*, 1997). These observations support a broken-then-healing cycle on the active fault. Nevertheless, the ratio of the waveguide width to the rupture length for both Hector Mine and Landers earthquakes is consistent with the scale of the dynamic process zone width to the fault length predicted by the cohesion-zone fault growth model (Cowie and Scholz, 1992), even though this model is appropriate for a single rupture on a simple slip-plane.

Locations of aftershocks showing fault-zone trapped waves reveal the multiple-fault rupture in the Landers and Hector Mine earthquakes. At Landers, the rupture is segmented by stepovers between pre-existing faults (Li *et al*, 1994a,b). At Hector Mine, the northern rupture zone bifurcates along two subparallel fault strands. The west slip plane of the northern rupture zone is on the Lavic Lake fault, which ruptured to the surface in the 1999 M 7.1 Hector Mine earthquake; the east slip-plane is on a buried fault that ruptured at seismogenic depth but without the surface expression. This bifurcation is also suggested by aftershock locations (Hauksson *et al.*, 2002) and by the study of the source process using strong-motion, telemetric, and surface deformation data (Dreger and Kaverina, 2000; Ji *et al.*, 2002a,b).

Acknowledgments

This study was supported by NSF Grant EAR-000132 and the Southern California Earthquake Center. SCEC is funded by NSF Cooperative Agreement EAR-8920136 and USGS Cooperative Agreements 14-08-0001-A0899 and 1434-HQ-97AG01718. Special acknowledgments to the Marine Corps Air Ground Combat Center (MCAGCC), Twentynine Palms, California, for their permission to carry out the experiment in the Base and their invaluable help when we deployed instruments in the Bullion Mountains. We thank L. Jones of the USGS for her coordination of our initial recording of trapped waves at the Hector Mine rupture zone and Karl Gross of the USGS for his coordination of our scientific activities in MCAGCC. We appreciate the support of IRIS-PASSCAL Instrument Center for the use of their instruments. We thank F. Bonilla, A. Bykvotsev, E. Cochran, P. Earle, V. Schulte-Pelkum, P. Shear, A. Tumarkin, L. Warren, and F. Xu for their work in the Bullion Mountains and the SCEC organization of instrument deployment through R. Archuleta, J. Steidl, and A. Martin. We also thank K. Hudnut, D. Dreger, M. Simons, S. Owen, and B. Graves for valuable discussions in this study. This work benefits from suggestions of the editor, M. Rymer, and two reviewers, A. Michael and K. Nishigami. The SCEC Contribution Number for this paper is 551.

References

Aki, K. (1984). Asperities, barriers, characteristic earthquakes, and strong motion prediction, *J. Geophys. Res.* **89,** 5867–5872.

Beck, S. L., and D. H. Christensen (1991). Rupture process of the February 4, 1965, Rat Islands earthquake, *J. Geophys. Res.* **96,** 2205–2221.

Ben-Zion, Y. (1998). Properties of seismic fault zone waves and their utility for imaging low-velocity structure, *J. Geophys. Res.* **103,** 12,567–12,585.

Blanpied, M. L., D. A. Lockner, and J. D. Byerlee (1992). An earthquake mechanism based on rapid sealing of faults, *Nature* **359,** 574–576.

Byerlee, J. (1990). Friction, overpressure and fault-normal compression, *Geophys. Res. Lett.* **17,** 2109–2112.

Chester, F. M., J. P. Evans, and R. L. Biegel (1993). Internal structure and weakening mechanisms of the San Andreas fault, *J. Geophys. Res.* **98,** 771–786.

Cowie, P. A., and C. H. Scholz (1992). Growth of faults by accumulation of seismic slip, *J. Geophys. Res.* **97,** 11,085–11,095.

Das, S., and K. Aki (1977). Fault plane with barriers: A versatile earthquake model, *J. Geophys. Res.* **82,** 5658–5670.

Dreger, D., and A. Kaverina (2000). Seismic remote sensing for the earthquake source process and near-source strong shaking: a case study of the October 16, 1999 Hector Mine earthquake, *Geophys. Res. Lett.* **27,** 1941–1944.

Ellsworth, W. L., (1990). Earthquake history, 1769–1989, in *The San Andreas Fault System, California*, R. E. Wallace (Editor), *U.S. Geol. Surv. Profess. Pap.* **1515,** 153–187.

Graves, R. W. (1996). Simulating seismic wave propagation in 3D elastic media using staggered-grid finite differences, *Bull. Seism. Soc. Am.* **86,** 1091–1106.

Harris, R. A., and S. M. Day (1993). Dynamics of fault interaction: parallel strike-slip faults, *J. Geophys. Res.* **98,** 4461–4472.

Hauksson, E., L. Jones, and K. Hutton (2002). The 1999 M_w 7.1 Hector Mine, California earthquake sequence: complex conjugate strike-slip faulting, *Bull. Seism. Soc. Am.* **92,** 1154–1170 (this issue).

Hough, S. E., Y. Ben-Zion, and P. Leary (1994). Fault-zone waves observed at the southern Joshua Tree earthquake rupture zone, *Bull. Seism. Soc. Am.* **84,** 761–767.

Ida, Y. (1973). The maximum acceleration of seismic ground motion, *Bull. Seism. Soc. Am.* **63,** 959–968.

Ji, C., D. J. Wald, and D. V. Helmberger (2002). Source description of the 1999 Hector Mine, California, earthquake. I. Wavelet domain inversion theory and resolution analysis, *Bull. Seism. Soc. Am.* **92,** 1192–1207 (this issue).

Ji, C., D. J. Wald, and D. V. Helmberger (2002). Source description of the 1999 Hector Mine, California, earthquake. II. Complexity of slip history, *Bull. Seism. Soc. Am.* **92,** 1208–1226 (this issue).

Johnson, A. M., R. W. Fleming, and K. M. Cruikshank (1994). Shear zones formed along long, straight traces of fault zones during the 28 June 1992 Landers, California, earthquake, *Bull. Seism. Soc. Am.* **84,** 499–510.

Jongmans, D., and P. E. Malin (1995). Microearthquake *S*-wave observa-

tions from 0 to 1 km in the Varian Well at Parkfield, California, *Bull. Seism. Soc. Am.* **85,** 1805–1820.

Leary, P. C., H. Igel, and Y. Ben-Zion (1991). Observation and modeling of fault zone seismic trapped waves in aid of precise precursory microearthquake location and evaluation, Presented at Conference on Earthquake Prediction: State-of-the-Art, Strasbourg, France, Oct. 15–18.

Lees, J. M., and P. E. Malin (1990). Tomographic images of *P* wave velocity variation at Parkfield, California, *J. Geophys. Res.* **95,** 21,793–21,804.

Li, Y. G. (2000). Mapping fault zones, IRIS *Newsl.* **2000** (1), 26.

Li, Y. G., and P. C. Leary (1990). Fault-zone trapped seismic waves, *Bull. Seism. Soc. Am.* **80,** 1245–1271.

Li, Y. G., and F. L. Vernon (2001). Characterization of the San Jacinto fault zone near Anza, California, by fault zone trapped waves, *J. Geophys. Res.* **106,** 30,671–30,688.

Li, Y. G., and J. E. Vidale (1996). Low-velocity fault-zone guided waves: numerical investigations of trapping efficiency, *Bull. Seism. Soc. Am.* **86,** 371–378.

Li, Y. G., and J. E. Vidale (2000). Trapped waves at the Lavic Lake fault ruptured in the *M* 7.1 Hector Mine, California, earthquake, *Geophys. Res. Lett.* **71,** 225.

Li, Y. G., and J. E. Vidale (2001). Healing of the shallow fault zone from 1994–1998 after the 1992 *M* 7.5 Landers, California, earthquake, *Geophys. Res. Lett.* **28,** 2999–3002.

Li, Y. G., K. Aki, D. Adams, A. Hasemi, and W. H. K. Lee (1994a). Seismic guided waves trapped in the fault zone of the Landers, California, earthquake of 1992, *J. Geophys. Res.* **99,** 11,705–11,722.

Li, Y. G., K. Aki, J. E. Vidale, and M. G. Alvarez (1998b). A delineation of the Nojima fault ruptured in the *M* 7.2 Kobe, Japan, earthquake of 1995 using fault-zone trapped waves, *J. Geophys. Res.* **103,** 7247–7263.

Li, Y. G., K. Aki, J. E. Vidale, and F. Xu (1999). Shallow structure of the Landers fault zone from explosion-generated trapped waves, *J. Geophys. Res.* **104,** 20,257–20,275.

Li, Y. G., P. C. Leary, K. Aki, and P. E. Malin (1990). Seismic trapped modes in the Oroville and San Andreas fault zones, *Science* **249,** 763–766.

Li, Y. G., F. L. Vernon, and K. Aki (1997). San Jacinto fault-zone guided waves: a discrimination for recently active fault strands near Anza, California, *J. Geophys. Res.* **102,** 11,689–11,701.

Li, Y. G., J. E. Vidale, K. Aki, C. J. Marone, and W. H. K. Lee (1994b). Fine structure of the Landers fault zone: segmentation and the rupture process, *Science* **256,** 367–370.

Li, Y. G., J. E. Vidale, K. Aki, and F. Xu (2000). Depth-dependent structure of the Landers fault zone using fault zone trapped waves generated by aftershocks, *J. Geophys. Res.* **105,** 6237–6254.

Li, Y. G., J. E. Vidale, K. Aki, F. Xu, and T. Burdette (1998a). Evidence of shallow fault zone strengthening after the 1992 *M* 7.5 Landers, California, earthquake, *Science* **279,** 217–219.

Malin, P. E., S. N. Blakeslee, M. G. Alvarez, and A. J. Martin (1989). Microearthquake imaging of the Parkfield asperity, *Science* **244,** 557–559.

Marone, C. (1998a). Laboratory-derived friction laws and their application to seismic faulting, *Annu. Rev. Earth Planet. Sci.* **26,** 643–696.

Marone, C. (1998b). The effect of loading rate on static friction and the rate of fault healing during the earthquake cycle, *Nature*, **391,** 69–72.

Michael, A. J., and D. M. Eberhart-Phillips (1991). Relations among fault behavior, subsurface geology, and three-dimensional velocity models, *Science*, **253,** 651–654.

Michelini, A., and T. V. McEvilly (1991). Seismological studies at Parkfield. I. Simultaneous inversion for velocity structure and hypocenters using cubic B-splines parameterization, *Bull. Seism. Soc. Am.* **81,** 524–552.

Papageorgiou, A. S., and K. Aki (1983). A specific barrier model for the quantitative description of inhomogeneous faulting and the prediction of strong motion. I. Description of the model, *Bull. Seism. Soc. Am.* **73,** 693–722.

Rice, J. R. (1980). The mechanics of earthquake rupture, in *Physics of the Earth's Interior*, A. M. Dziewonski and E. Boschi (Editors), North-Holland, Amsterdam, 555–649.

Rice, J. R. (1992). Fault stress states, pore pressure distributions, and the weakness of the San Andreas fault, in *Fault Mechanics and Transport Properties of Rocks*, B. Evans and T.-F. Wong (Editors), Academic Press, San Diego, California, 475–503.

Scholz, C. H. (1990). *The Mechanics of Earthquakes and Faulting*, Cambridge Univ. Press, New York.

Scientists of the U.S. Geological Survey, Southern California Earthquake Center, and California Division of Mines and Geology (2000). Preliminary report on the 16 October 1999 *M* 7.1 Hector Mine, California, earthquake, *Seismo. Res. Lett.* **71,** 11–23.

Sibson, R. H. (1977). Fault rocks and fault mechanisms, *J. Geol. Soc. Lond.* **133,** 191–213.

Sieh, K., L. Jones, E. Hauksson, K. Hudnut, D. Eberhart-Phillips, T. Heaton, S. Hough, K Hutton, H. Kanamori, A. Lilji, S. Lindvall, S. McGill, J. Mori, C. Rubin, J. Spotila, J. Stock, H. Thio, J. Treiman, B. Wernick, and J. Zachariasen (1993). Near-field investigations of the Landers earthquake sequence, April to July 1992, *Science* **260,** 171–176.

Simons, M., Y. Fialko, C. Ji, L. Rivera (2000). Co-seismic static deformation from the 16 October 1999 *M* 7.1 Hector Mine CA earthquake, *Eos Trans. AGU Fall Meet. Suppl.* **81** (48), F839.

Thurber, C. H., S. Roecker, W. Ellsworth, Y. Chen, W. Lutter, and R. Sessions (1997). Two-dimensional seismic image of the San Andreas fault in the northern Gabilan Range, central California: evidence for fluids in the fault zone, *Geophys. Res. Lett.* **24,** 1591–1594.

Treiman, J. A., K. J. Kendrick, W. A. Bryant, T. K. Rockwell, and S. F. McGill (2002). Primary surface rupture associated with the M_w 7.1 16 October, 1999 Hector Mine earthquake, San Bernardino County, California, *Bull. Seism. Soc. Am.* **92,** 1171–1191 (this issue).

Vidale, J. E., W. L. Ellsworth, A. Cole, and C. Marone (1994). Rupture variation with recurrence interval in eighteen cycles of a small earthquake, *Nature* **368,** 624–626.

Wald, D. J., and T. H. Heaton (1994). Spatial and temporal distribution of slip for the 1992 Landers, California, earthquake, *Bull. Seism. Soc. Am.* **84,** 668–691.

Department of Earth Sciences
University of Southern California, Los Angeles, CA 90089-0740
ygli@terra.usc.edu
(Y.G.L.)

Department of Earth and Space Sciences
University of California, Los Angeles, CA 90095
vidale@moho.ess.ucla.edu
(J.E.V.)

Department of Geological Sciences
San Diego State University, San Diego, CA 92182
day@moho.sdsu.edu
(S.M.D.)

Department of Earth Sciences
University of Riverside, Riverside, CA 92521
david.oglesby@ucr.edu
(D.D.O.)

Manuscript received 18 October 2000.